



Full Length Article

Study on charge storage mechanism in working electrodes fabricated by sol-gel derived spinel NiMn₂O₄ nanoparticles for supercapacitor application



Apurba Ray^a, Atanu Roy^a, Monalisa Ghosh^b, Jesús Alberto Ramos-Ramón^c, Samik Saha^a, Umapada Pal^c, Swapan Kumar Bhattacharya^d, Sachindranath Das^{a,*}

^a Department of Instrumentation Science, Jadavpur University, Kolkata 700032, India

^b Instrumentation and Applied Physics, Indian Institute of Science, Bangalore 560012, India

^c Instituto de Física, Benemérita Universidad Autónoma de Puebla, Apdo. Postal J-48, Puebla 72570, Mexico

^d Physical Section, Department of Chemistry, Jadavpur University, Kolkata 700032, India

ARTICLE INFO

Keywords:

EIS
Electrode material
Energy storage
NiMn₂O₄ nanoparticle
Supercapacitor

ABSTRACT

We report the synthesis of porous spinel-structured binary NiMn₂O₄ metal oxide nanoparticles and their performance as electrode material for supercapacitors. Spherical NiMn₂O₄ nanoparticles of ~8 nm average diameter have been synthesized using inexpensive and simple sol-gel method, and characterized by X-ray diffraction, field emission scanning electron microscopy, X-ray photoelectron spectroscopy, and Fourier transform infrared spectroscopy. The electrodes made of this single phase spinel nanoparticles exhibit superior electrochemical performance with excellent rate capability, offering highest specific capacitance value of 875 F g⁻¹ at 2.0 mV s⁻¹ scan rate in 1 M Na₂SO₄ electrolyte solution. Furthermore, an asymmetric supercapacitor is also assembled and possesses a wide operating voltage window of 1.8 V, exhibiting an energy density of 75.01 Wh kg⁻¹ at a power density of 2250.91 W kg⁻¹. The results infer this highly porous binary metal oxide nanostructures are promising candidates for high performance energy storage applications.

1. Introduction

Recently, supercapacitors, also known as electrochemical capacitors or ultracapacitors, have become attractive alternatives to other energy storage systems such as commercial batteries, fuel cells, etc. due to their excellent electrochemical performances like high power density, long cycle life, fast charge-discharge rate, safety and environmental friendliness [1–6]. Based on energy storage mechanism, supercapacitors can be divided into two categories: (i) Electric double-layer capacitors (EDLC), in which charge accumulates at the interface of electrode and electrolyte through electrostatic process, i.e. non-Faradic process. Generally, carbon-based materials such as carbon nanotubes (CNTs), activated carbon (AC), graphene, etc. have been explored as electrode materials for EDLCs [7–14]. (ii) The other type of supercapacitors are known as pseudocapacitors, in which energy storage is achieved by redox reactions or intercalation of specific ions at the surface of electrode, resulting in a reversible Faradaic charge-transfer on the electrode. Various transition-metal oxides like RuO₂, NiO, V₂O₅, Fe₂O₃, Co₃O₄, MnO₂ etc. have been investigated as promising electrode materials for supercapacitor applications [15–23]. Among them, RuO₂ has been studied extensively, especially for military applications, because

of its most preferable properties such as excellent reversibility, high specific capacitance, high proton conductivity, good thermal stability, long cycle-life etc. However, low natural abundance, high cost, and toxic nature are some of the limitations of RuO₂ for large scale application and commercialization, initiating a strong enticement for the search of inexpensive and promising alternatives of RuO₂. Although a large number of metal oxides have been tested, and a great fraction of them exhibited high specific capacitance with good redox reaction performances; frequently, high electrical resistivity of these metal oxides makes them unsuitable for application in supercapacitor electrodes.

Hence, there is a strong motivation and enticement to search inexpensive and promising alternative electrode materials to replace RuO₂. Many metal oxides have exhibited high specific capacitance values with their redox reaction performances but high resistivity of the metal oxides electrodes is seem to be a great challenged for their device applications [24–26]. On the other hand, it is reported that the electrical conductivity of metal oxide for pseudocapacitor application can be increased by hosting impurities, via sintering in selective gaseous environment or through doping. Mixing one metal oxide material with other, i.e. forming a binary or ternary metal oxide, has been well

* Corresponding author.

E-mail address: sachindran.das@jadavpuruniversity.in (S. Das).

<https://doi.org/10.1016/j.apsusc.2018.08.259>

Received 26 May 2018; Received in revised form 27 August 2018; Accepted 30 August 2018

Available online 31 August 2018

0169-4332/ © 2018 Elsevier B.V. All rights reserved.

established as one of the best solutions to improve the electrical conductivity of the electrode material. Such mixed oxides of good electrical conductivity enhance the charge transfer process at the electrode-electrolyte interface, aiding the charge transportation towards current collector, enhancing the charge storage performance of the supercapacitor. Nanostructures of different transition metal ternary oxides such as MnFe_2O_4 , ZnFe_2O_4 , CuFe_2O_4 , CoFe_2O_4 , NiCo_2O_4 and $\text{NiCo}_2\text{O}_4@ \text{MnO}_2$ core-shell, $\text{Co}_3\text{O}_4@ \text{MnO}_2$ core-shell, NiO/Ni core-shell, Ni-Co double hydroxide and $\alpha\text{-MnO}_2/\delta\text{-MnO}_2$ Core-Shell are considered to be some promising high performance supercapacitors electrode materials [27–32]. Recently, single phase spinel-structured NiMn_2O_4 , a low cost, non-toxic ternary metal oxide, has received a great interests over many other metal oxides due to its excellent electrochemical performance [33–37]. As has been stated earlier, to be used as electrodes in supercapacitors, materials with good electrical conductivity and excellent electrochemical performance are needed for achieving high energy density and high power density. In this context, nanostructured materials are more suitable than traditional bulk materials as electrode materials for supercapacitor, as they offer higher surface to volume ratio and shorter electron-ions transport channels. In fact, metal oxide nanostructures become the target of modern research for their utilization in high performance energy storage devices. Moreover, the morphology of those nanostructures is seen to improve their electrochemical performance. Therefore, designing metal oxide nanostructures of controlled morphology and size with good electrical conductivity is a challenge for their utilization in energy storage devices such as electrochemical supercapacitors [38–41].

In this work, we report on the synthesis mesoporous NiMn_2O_4 nanoparticles through a simple, one-pot sol-gel process, and their electrochemical properties in a redox active Hydroquinone (HQ) incorporated aqueous 1 M Na_2SO_4 electrolyte solution, to evaluate the possibility of their application as energy storage electrode material in supercapacitors. Here, The addition of redox active species HQ to the Na_2SO_4 electrolyte enhances the fast redox reactions on the surface of the electrode as well as improves the charge storage capacity of the electrode via its electrochemical redox behavior. It enhances the current rate during charge- discharge process due to the occurrences of a quasi-reversible chemical reaction (oxidation/reduction) between the Hydroquinone (HQ)-quinone (Q) couples particularly at the counter electrode. During charging, HQ is oxidized to Q by generation of 2H^+ with 2e^- and Q is reduced to HQ via adsorption of 2H^+ with 2e^- during discharge. Through electrochemical impedance spectroscopy (EIS) study, we demonstrate the fabricated NiMn_2O_4 nanoparticles exhibit good electrochemical response with smart long cycle capability and can be considered as auspicious aspirant pseudocapacitor electrode material for high performances supercapacitors applications.

2. Experimental

2.1. Synthesis procedure

For the synthesis of NiMn_2O_4 nanoparticles, first 1.0 mM of Ni $(\text{CH}_3\text{COO})_2 \cdot 4\text{H}_2\text{O}$ and 2.0 mM of Mn $(\text{CH}_3\text{COO})_2 \cdot 4\text{H}_2\text{O}$ were dissolved in 70 mL of ethylene glycol under magnetic stirring for 10 min. Then 0.15 g of polyvinyl pyrrolidone (PVP, $(\text{C}_6\text{H}_9\text{NO})_n$) was added into the solution and kept under continuous magnetic stirring for 20 min to obtain a homogeneous transparent solution. The resulting mixture was transferred to 100 mL round bottom flask, and put on a hot oil-bath under magnetic stirring. The temperature of the oil-bath was increased to 175 °C and kept at this temperature for 4 h. After cooling to room temperature, the precipitate was repeatedly washed with ethanol and distilled water, and finally collected by centrifugation at 8000 rpm. Then obtained sample was dried at 90 °C for 48 h. Finally, the as-prepared sample was air-annealed at 400 °C for 4 h (at 2 °C/min heating rate) inside a muffle furnace to obtain NiMn_2O_4 nanoparticles in powder form.

2.2. Materials characterization

The crystallinity and phase structure of the NiMn_2O_4 nanoparticle were analyzed through powder X-ray diffraction in the 20–80° range, using $\text{CuK}\alpha$ radiation ($\lambda = 1.542 \text{ \AA}$ generated at 40 kV and 40 mA) of a Rigaku miniflex-600 bench top diffractometer. The size and surface morphology of the prepared NiMn_2O_4 nanostructures were investigated in a JEOL JSM 6700F (Japan) Field emission scanning electron microscope (FESEM). The morphological analysis of this NiMn_2O_4 nanoparticles were executed using high resolution transmission microscope (HRTEM) (FEI, TF30-ST) operated at 200 kV. Fourier transform infrared (FTIR) spectrum of the sample was recorded in a RX1 Perkin Elmer FTIR spectrometer, using KBr pellets as reference. X-ray photoelectron spectroscopy (XPS) analysis of the sample was carried out in a SPECS GmbH spectrometer (Phoibos 100 MCD analyzer) using $\text{MgK}\alpha$ radiation (1253.6 eV). The recorded spectra were corrected using the binding energy of carbon (C1s, 284.6 eV). XPS signals were analyzed by CASA XPS software. The specific surface area and porosity of the powder sample were estimated through their N_2 adsorption-desorption characteristics at 77 K, utilizing a Belsorp Mini II (BEL, Japan) sorptometer. The specific surface areas (S_g) of the sample were estimated using BET analysis. The sample was degassed at 250 °C for 10 h before recording its physisorption isotherms. The technique of back extrapolation of the linear portion of the isotherms to zero equilibrium pressure was used to determine the saturation uptake.

2.3. Microstructural analysis by Rietveld refinement

The structure and microstructure characterization of the prepared powder NiMn_2O_4 nanocrystal were performed by analyzing the XRD pattern by Rietveld's whole profile fitting method employing the MAUD software version 2.26. Different microstructural parameters were obtained from this technique. The Marquardt least-squares procedure was implemented for minimizing the difference between the observed and refined diffraction patterns. Pseudo-Voigt (PV) function was used to calculate the microstrain and lattice parameter. The refinement was continued until the goodness of fitting (GoF) approaches unity and the quality of fitting was observed using reliability index parameter, R_{wp} (weighted residual error) and R_{exp} (expected error). R_{wp} and R_{exp} can be defined as,

$$R_{wp} = \left[\frac{\sum_i W_i (I_o - I_c)^2}{\sum_i W_i (I_o)^2} \right]^{1/2}$$

$$R_{exp} = \left[\frac{(N-P)}{\sum_i W_i (I_o)^2} \right]^{1/2}$$

where I_o and I_c were the observed and refined intensities, W_i and N were the weight and number of observations and P was the number of refined parameters [42–47]. The value of the goodness of fitting (GoF) was calculated using the expression

$$GoF = \frac{R_{wp}}{R_{exp}}$$

2.4. Electrochemical measurement

The electrochemical performances of NiMn_2O_4 electrode material was studied in a CS313 (CorrTest, China) multi-channel electrochemical workstation at room temperature using Cyclic Voltammetry (CV), Galvanostatic charge-discharge (GCD), and Electrochemical Impedance Spectroscopy (EIS) methods. All the measurements were carried out in conventional three electrodes assembly, where platinum (Pt) electrode (1 cm × 1 cm) was used as the counter electrode and Ag/AgCl in saturated KCl solution as a reference electrode. To prepare the working electrodes, Teflon-coated graphite rod was used as a current

collector. The active working electrode material was prepared by mixing NiMn₂O₄ nanoparticles (85 wt%), graphite powder (10 wt%) and polyvinylidene fluoride (PVDF, 5 wt%) in 200 μ L N-Methylpyrrolidone (NMP) solution under sonication (30 min), obtaining a gel. The gel was then drop casted on the one flat end of the Teflon coated graphite rod and dried in vacuum at 333 K for 6 h. The mass of the active electrode material in each electrode was about 0.5–1.0 mg (4–8 mg cm⁻²). The CV measurements were carried out in 0.01 M Hydroquinone (HQ) mixed 1.0 M Na₂SO₄ solution as electrolyte. The small amount of redox active species Hydroquinone (HQ) was mixed with 1.0 M Na₂SO₄ electrolyte solution to enhance the fast redox reaction at the surface of working electrode [48–50]. The specific capacitance (C_m) was calculated from the cyclic voltammetry (CV) curve using Eq. (1)

$$C_m = \frac{i}{2mv} \quad (1)$$

where m and v are the mass of the electroactive material and potential scan rate, respectively. Current (i) was obtained by integrating the area of the curves using Eq. (2),

$$i = \int i(v)dv/(v_c - v_a) \quad (2)$$

where v_a and v_c are the lowest and highest voltage of the potential range, respectively [2,7,51–53].

2.5. Fabrication of asymmetric supercapacitor

To further investigate the electrochemical performance of spinel NiMn₂O₄ nanocomposite for practical supercapacitor device applications, asymmetric supercapacitor (ASC) device was fabricated and studied in two-electrode test system with 1 M Na₂SO₄ as the electrolyte. The prototype ASC device was assembled using as synthesised NiMn₂O₄ nanocomposites and commercially available activated carbon (AC) as positive and negative electrodes, respectively. The negative electrode was prepared by 90 wt% activated carbon (AC) and 10 wt% PVDF binder dispersed in NMP solution to produce a homogeneous paste. This paste was then coated uniformly on one side onto the steel plate (2 cm \times 3 cm). The prepared electrodes were dried at 330 K for 5 h. All the electrochemical studies of ASCs were carried out at 300 K using same procedure and the energy density (E_{cell}) (Wh kg⁻¹) and power density (P_{cell}) (W kg⁻¹) of the device were calculated on the total mass of the active materials by following the Eqs. (3)–(5) [54,55].

$$C_s = \frac{I \times \Delta t}{m \times (V_f - V_i)} \quad (3)$$

$$E_{cell} = \frac{1}{2} \left[\frac{C_s (V_f - V_i)^2}{3.6} \right] \quad (4)$$

$$P_{cell} = \frac{3600 \times E_{cell}}{\Delta t} \quad (5)$$

where C_s is the calculated specific capacitance of the ASC devices (F g⁻¹), I is the discharge current (A), Δt is the discharge time (s), m is the mass of the active electrode (g) and $(V_f - V_i)$ is the potential window for discharge process (V).

3. Results and discussion

3.1. Material characterization

The typical powder X-ray diffraction (XRD) pattern (black line) of the NiMn₂O₄ nanoparticles with refined patterns (red bubble) and their differences (blue line) is shown in Fig. 1(a). All the observed peaks are found to be well consistent with standard NiMn₂O₄ patterns (JCPDS no. 71-0852) [56–58]. The diffraction peaks revealed at $2\theta = 18.56^\circ$, 30.56° , 35.98° , 43.65° , 57.29° , 63.26° and 74.55° correspond to the

(1 1 1), (2 0 0), (3 1 1), (4 0 0), (5 1 1), (4 4 0) and (5 3 3) planes of NiMn₂O₄, with interplaner spacing d of 4.7765, 2.9228, 2.5061, 2.109, 2.099, 1.876 and 1.716 Å, respectively. The positions of all the diffraction peaks matched well with the standard single phase spinel structure (face centered cubic) of NiMn₂O₄ of space group Fd-3m as shown in Fig. 1(b) constructed by the data obtained from XRD analysis using VESTA software package [33–35,56,59,60]. The NiMn₂O₄ spinel structure composed of octahedral Mn³⁺ and tetrahedral Ni²⁺. The octahedral Mn³⁺ is linked through edges. The goodness of fitting (GoF) obtained from Rietveld refinement is 0.881 which is close to 1.0 signifies that the fitting quality is relatively good. There is no other peak present in the diffraction pattern, which confirms the purity of the NiMn₂O₄ phase [36,37,61–63]. However, the revealed XRD peaks of the sample are broad, probably due to smaller grain size of the nanostructures. The average crystallite size of the sample estimated using the well-known Scherrer equation was about 7.0 nm. As can be observed from the FESEM micrograph (Fig. 1c), densely packed agglomerated spherical NiMn₂O₄ nanoparticles of 6–10 nm size range (\sim 8 nm average size) were formed. Formation of such densely packed small NiMn₂O₄ nanoparticles effectively generates porous surface of high specific surface area, which enhances the electrochemical performance of the electrodes made of them due to high contact area of the material with electrolyte. To describe the morphological, compositional and porous nature of this NiMn₂O₄ material, TEM images of the sample is shown in Fig. 1(d). The image shows the interconnected nanoparticles framework with mesoporous structure, and the pores are homogeneously distributed among the whole sample.

Fig. 2 presents the FTIR spectrum of the as prepared NiMn₂O₄ nanostructures in the range 4000–400 cm⁻¹. The broad absorption band appeared in between 3000 and 3500 cm⁻¹ correspond to the stretching vibration of O-H group coming from H₂O molecules physi-adsorbed on the surface of the material. Such surface adsorbed H₂O molecules enhance the wettability of the electrode, which leads to improve the electrochemical performance of the electrode material. The strong absorption band centered around 1402 cm⁻¹ corresponds to the stretching vibration of CO₂ coming from the atmosphere. The main two characteristic bands observed around 400 and 600 cm⁻¹ in the FTIR spectrum correspond to the vibrational modes of octahedral Ni²⁺–O²⁻ and tetrahedral Mn³⁺–O²⁻ groups, respectively. Appearance of these two characteristic absorption bands in the FTIR spectrum of the nanostructures confirms further their single phased spinel structure. Finally, the weak absorption band appeared in between 2300 and 380 cm⁻¹ corresponds to the C-O stretching vibration appearing either from the atmospheric CO₂ or residual ethylene glycol. No other organic functional group could be detected in the FTIR spectrum of the nanostructures [36].

The compositions and chemical state of the elements in the NiMn₂O₄ nanoparticles have been analyzed further by XPS (Fig. 3(a–d)). The XRS survey spectrum (Fig. 3(a)) revealed only the presence of Ni, Mn and O in the sample, without any other impurity. The high resolution XPS spectrum of Ni 2p (Fig. 3(b)) revealed spin-orbit doublet, with peaks at binding energies 854.8 eV and 872.6 eV, correspond to Ni 2p_{3/2} and Ni 2p_{1/2} states (separated by 17.74 eV), with satellite peaks around 861.1 and 879.1 eV, respectively. These peaks also consist of two sub-components which confirm the presence of Ni²⁺ state (around 855.4 and 873.1 eV) and Ni³⁺ state (around 857.3 and 875.5 eV) in NiMn₂O₄. Similarly, the Mn 2p spectrum also revealed peaks with binding energies 640.2 eV and 651.4 eV, correspond to Mn 2p_{3/2} and Mn 2p_{1/2}, respectively (Fig. 3(c)) [64–68]. Gaussian deconvolution of Mn 2p emission revealed four component bands (Fig. 3(c)). While the 639.9 and 651.2 eV component bands could be assigned to Mn in Mn²⁺ state, the other two component bands at 641.7 eV and 653.2 eV correspond to Mn in Mn³⁺ state. As expected, a deconvolution of the O 1s band revealed 3 components (Fig. 3(d)), appearing around 529.75, 530.93, and 533.51 eV. While the component revealed at 533.51 eV correspond to surface adsorbed oxygens (O_{ads}, i.e. O₂⁻, O⁻,

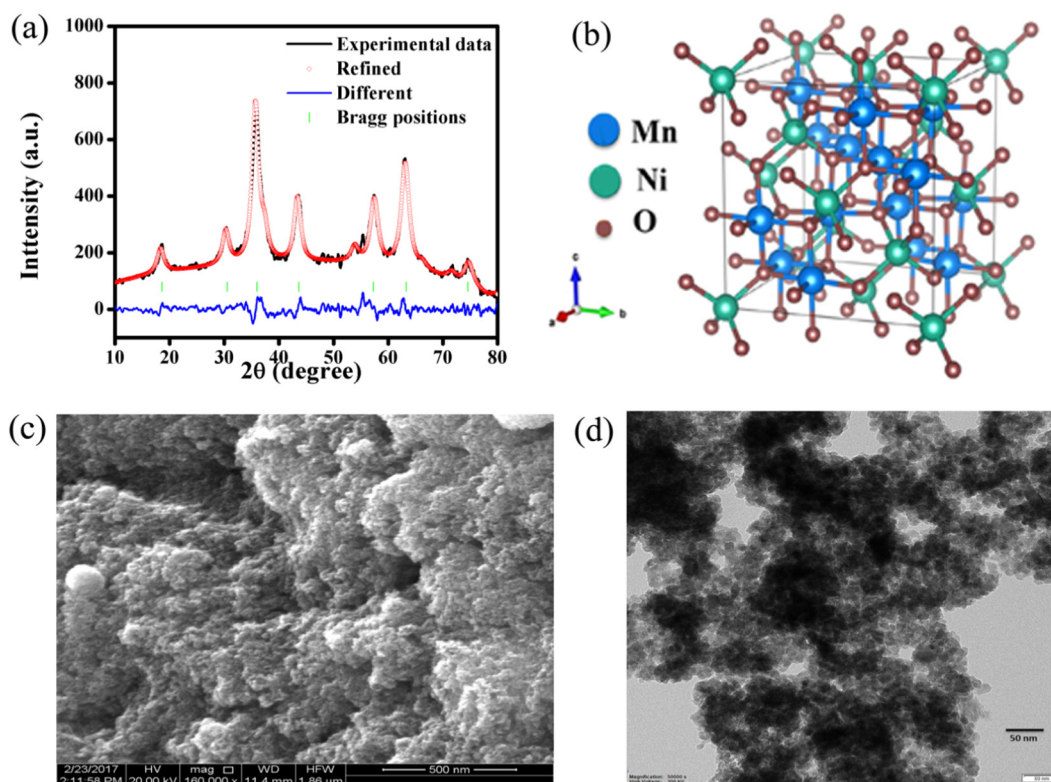


Fig. 1. (a) The Rietveld refinement of XRD pattern, (b) spinel structure of NiMn_2O_4 , (c) FESEM image and (d) TEM image of NiMn_2O_4 nanoparticles.

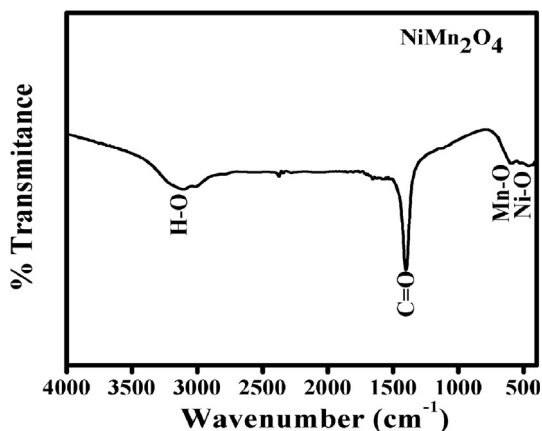


Fig. 2. FTIR spectrum of NiMn_2O_4 nanoparticle.

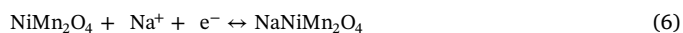
OH^- species), the components revealed at 529.75 and 530.93 eV correspond to lattice oxygen (O_β i.e. O^{2-} ions). Quantitative XPS analysis confirms the presence of Ni and Mn in atomic ratio Ni:Mn = 1:2 (calculated by CASA XPS software) and the formation of pure spinel NiMn_2O_4 nanostructures. [33,37,69–72].

The porous nature of the NiMn_2O_4 nanostructures was confirmed from their nitrogen adsorption-desorption isotherm and the Brunauer-Emmett-Teller (BET) surface area measurement [73–76]. The adsorption-desorption plots of the sample presented in Fig. 4 clearly revealed a typical type IV isotherm, correspond to the mesoporous nature of NiMn_2O_4 nanocrystals. The BET estimated specific surface area of the material was $43.6 \text{ m}^2 \text{ g}^{-1}$ which offered large number of active sites in the electrochemical process. Such a high specific surface area of the nanostructures can also provide a large contact area between the electrolyte solution and the electrode made of them, ensuing fast ion transfer at the interface. The BJH pore size distribution of the sample presented as inset of Fig. 4 revealed an average pore size of 13.3 nm,

confirming its mesoporous nature. The wide pore size distribution of the nanostructures is also advantageous for their applications as electrode material due to easy accessibility of electrolyte solution and hence enhanced electron and ion exchange during the charge/discharge process [3,77–80].

3.2. Electrochemical properties

The cyclic voltammogram (CV) curves (Fig. 5(a)) of the NiMn_2O_4 electrode at various scan rates (2, 5, 10, 20, 40, 60, 80 and 100 mV s^{-1}) in the potential range -1.0 to 1.3 V indicate the typical Faradic charge transfer behaviour due to the presence of functional groups or pore size distribution. No additional O_2 or H_2 gas evolution observed at the edges of higher working potential window (-1.0 V to 1.3 V), which implies that the NiMn_2O_4 nanomaterial electrodes can perform in this wide potential range without degradation [2,81]. The non-rectangular shape of the CV curves specifies the redox nature of the electrode material and provides the information on the pseudocapacitive behaviour of the electrode in a suitable electrolyte solution. There appeared several oxidation and reduction peaks ($\text{Mn}^{3+} \leftrightarrow \text{Mn}^{4+}$ and $\text{Ni}^{2+} \leftrightarrow \text{Ni}^{3+}$) in the CV curves, which can be clearly identified due to the faradic redox processes related to Eq. (6) [35,36,79]



From this equation (Eq. (6)) it is clear that Na^+ ions from Na_2SO_4 electrolyte diffuse into the NiMn_2O_4 electrode material ($\sim 0.36 \text{ V}$ vs Ag/AgCl) and absorb one electron per ion during charging time. Subsequently, during discharging Na^+ ions are released from electrode material ($\sim 0.28 \text{ V}$ vs Ag/AgCl) to electrolyte solution and one electron per ion is released to the external circuit. Here Na ions are working as charge compensation agent to enhance the capacitive performance of the NiMn_2O_4 electrode [82]. As can be observed in Fig. 5(a), with the increase of potential scan rate, the peak associated to oxidation and reduction potential shift towards positive and negative potential, respectively. On increasing the scan rate, applied voltage with respect to

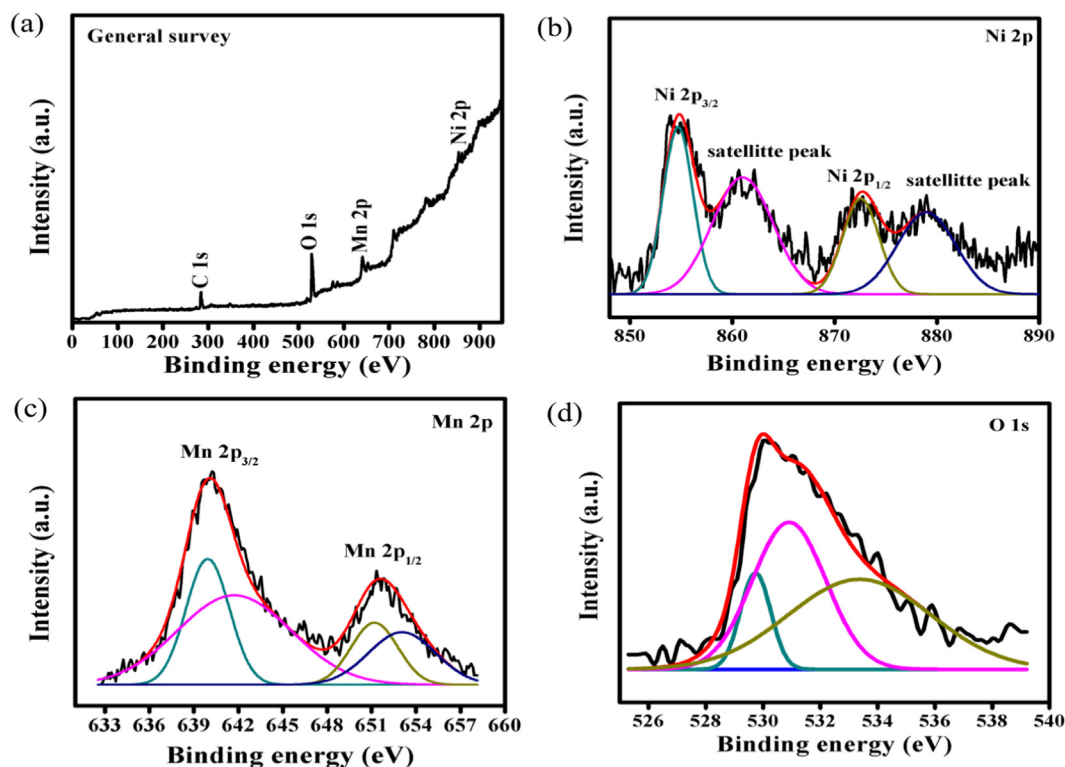


Fig. 3. The XPS spectra of NiMn_2O_4 nanoparticles (a) survey spectrum, (b) Ni 2p, (c) Mn 2p and (d) O 1s.

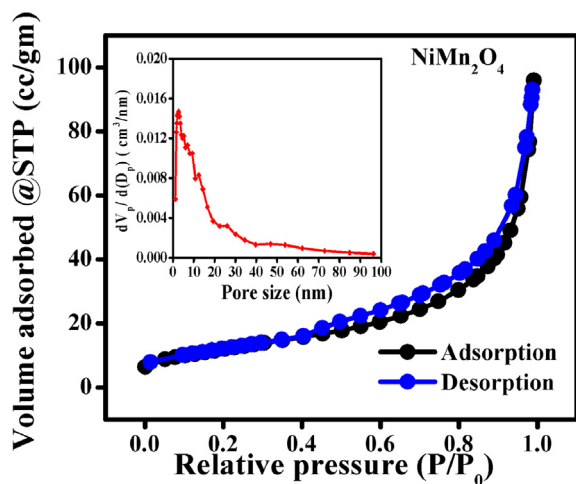


Fig. 4. Nitrogen adsorption/desorption isotherms with pore size distribution (inset) of NiMn_2O_4 nanoparticles.

the reference electrode (Ag/AgCl) increases faster. As a result, all the portions of the working electrode do not get enough time to undergo oxidation and redox reactions. Therefore, at higher scan rates, charge transfer at the interface (electrode-electrolyte) is limited by Sparran kinetics, and more work is required to reduce the system completely. It has been observed that, the oxidation and reduction peaks become more conspicuous due to the addition of redox active species Hydroquinone (HQ) in electrolyte solution, which stipulates that the extensive redox reaction follow at the surface of the electrode material (see Supplementary Fig. S1(a)). Thus, the total amount of charge stored in the NiMn_2O_4 electrode due to redox reaction can be calculated from the area covered by the current-voltage curve, i.e. CV curve at a fixed scan rate. All the recorded CV curves (Fig. 5(a)) indicate an increase in current density with the increase of scan rate, without any significant change in the nature of CV curve, indicating a high stability of the

electrode. The specific capacitance (C_m) of the electrode for each scan rate has been calculated from the CV curves by using Eqs. (1) and (2) and the maximum specific capacitance of 875 F g^{-1} was obtained at a scan rate 2 mV s^{-1} . The variation of specific capacitance of the electrode with scan rate is demonstrated in Fig. 5(b). As can be seen, the specific capacitance initially decreases sharply with the increase of scan rate, and then decreases very slowly at high scan rates. The variation of capacitance value with scan rate can be explained on the basis of movement of ions from electrolyte to electrode material. The charge storage capability of the electrode material is generally followed its electro-oxidation and reduction process. The oxidation of the working electrode takes place through the subtraction of electrons from the electrode material and diffusion of anions from the electrolyte solution to counter balance the developed positive charge, maintaining charge neutrality.

At lower scan rates, the ions from Na_2SO_4 electrolyte solution need longer time to access the outer and inner surface of the electrode, which leads to the accumulation of a large number of ions at the surface of active electrode, enhancing its charge storage capacity (enhanced capacitance). However, at higher scan rate, due to higher mobility and slow diffusion of redox electrolyte, the electrolyte ions can access only the outer surface of the electrode. As a result only a few ions get accumulated at the outer surface of the electrode, reducing the specific capacitance value. Thus the reduction of the rate performance of the capacitor at high scan rate is also related to the reduction of the electrolyte, not only related to the NiMn_2O_4 electrode material. The obtained results clearly indicate that the specific capacitance of a porous electrode strongly depends on applied scan rate. The specific capacitance value decreases with increase of scan rates, disclosing the specific capacitance value of an electrode material is strongly depend on the applied scan rates. Normally, the cyclic voltammetry (CV) current of an electrode material is the combination of both Faradic adsorption/desorption i.e. redox current and non-Faradic capacitive current, which can be clearly explained according to the Power law [83–85]. Thus, the total amount of charge stored in the electrode can be divided into three distinct components: the Faradic contribution from Na^+ ion insertion

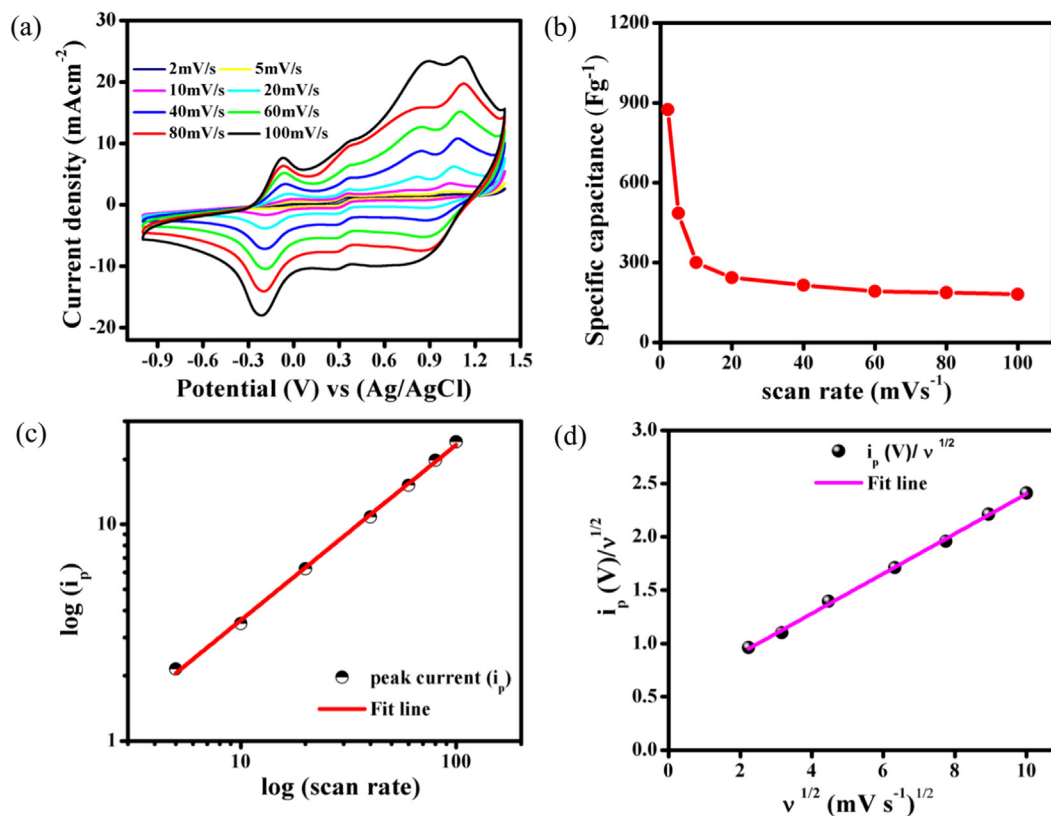


Fig. 5. (a) Cyclic voltammetry (CV) curves at different scan rates, (b) Specific capacitance vs scan rate, (c) $\log(i_p)$ vs $\log(\text{scan rate})$ and (d) $i_p/\nu^{1/2}$ vs $\nu^{1/2}$ plot of NiMn₂O₄ nanoparticles.

process, the Faradic contribution from the charge transfer process at surface atoms, known as pseudocapacitance effect, and the non-Faradic double layer effect. Double layer effect and pseudocapacitive effect become prominent when the particle size of the electrode material reduces to nanoscale dimension (less than 50 nm) due to high exposed surface area. Hence, the scan rate dependence CV current of an electrode can be expressed as Eq. (7)

$$i_p = a \nu^b \quad (7)$$

where ν is the scan rate (mV s^{-1}), a and b are the adjustable parameters. The ‘ b ’ value can be calculated from the slope of $\log(i_p)$ vs $\log(\nu)$ plot at a fixed potential (V). It is well known that, for ideal diffusion controlled Faradic process of ions, the slope $b = 0.5$ and the peak current i_p is proportional to the square root of the scan rate. Therefore, the peak current can be expressed by Eq. (8)

$$i_p = 0.4958 nFACD^{1/2} \left(\frac{\alpha nF}{RT} \right)^{1/2} \nu^{1/2} \quad (8)$$

where n represents the electron number, F is the Faraday constant, A is the effective surface area of working electrode, C is the maximum concentration of Na^+ in the lattice, α is the transfer coefficient, R is the ideal gas constant, T is the temperature in Kelvin, and D is the diffusion coefficient of Na^+ ions. On the other hand, for non-Faradic capacitive current, i.e. for non-diffusion controlled process, the value of the slope $b = 1$, and then the peak current (i_p) follows the linear scan rate dependence expression Eq. (9)

$$i_p = AC_d \nu \quad (9)$$

where A is the total electrode surface area, and C_d is the amount of capacitive storage per electrode surface area. Fig. 5(c) shows the plot of scan rate dependence peak current $\log(i_p)$ vs $\log(\nu)$. The best linear fit of the data to an apparent power law gives the b value of 0.71 (the maximum peak current has been considered), which can apparently be

ascribed to a mixed process involving both the insertion of Na^+ ions within the bulk of NiMn₂O₄ nanoparticles, and the capacitive storage of Na^+ ions at the outer surface of the electrode. Thus, the relative contribution of Na^+ ions in the adsorption/desorption current and capacitive current for a fixed potential can be quantified using Eq. (10)

$$i_p(V) = k_1 \nu + k_2 \nu^{1/2} \quad (10)$$

where $i_p(V)$ presents the peak current at a given potential, k_1 and k_2 are constants, and ν is the scan rate. The product $k_1 \nu$ denotes the contribution of capacitive current (i_c) for a fixed $di_p(V)/d\nu$, and $k_2 \nu^{1/2}$ provides the diffusion controlled current (i_d) or redox reaction current for a fixed $di_p(V)/d\nu^{1/2}$. The parameter k_1 can be determined from the product AC_d of Eq. (9), while the parameter k_2 can be determined from the product $0.4958 nFACD^{1/2} (\alpha nF/RT)^{1/2}$ of Eq. (8). Now, we can divide both the sides of Eq. (10) by $\nu^{1/2}$ to obtain Eq. (11)

$$\frac{i_p}{\nu^{1/2}} = k_1 \nu^{1/2} + k_2 \quad (11)$$

The values of k_1 and k_2 can be determined from $i_p(V)/\nu^{1/2}$ vs $\nu^{1/2}$ plots. The slope and intercept of the linear fit correspond to the value of k_1 and k_2 , which can quantitatively estimate the contributions of capacitive current (i_c) and diffusion current (i_d) at a fixed potential. Fig. 5(d) shows the plot of $i_p(V)/\nu^{1/2}$ vs $\nu^{1/2}$ and the linear fit line correspond to the value of k_1 ($k_1 = 0.18699$) and k_2 ($k_2 = 0.53287$). Therefore, it can be proposed that the charge stored in the electrode is mainly contributed by the Faradic adsorption/desorption through redox charge transfer process, rather than capacitive mechanism, as has been well demonstrated by the ‘ b ’ value from the CV curves using Power law [24,85,86].

A similar analysis proposed by Trasatti, et al. designates the relationship between the specific capacity and the scan rate. The total specific capacitance of an electrode is the combination of two specific capacitances, contributed by the inner surface (C_{in}) and the outer

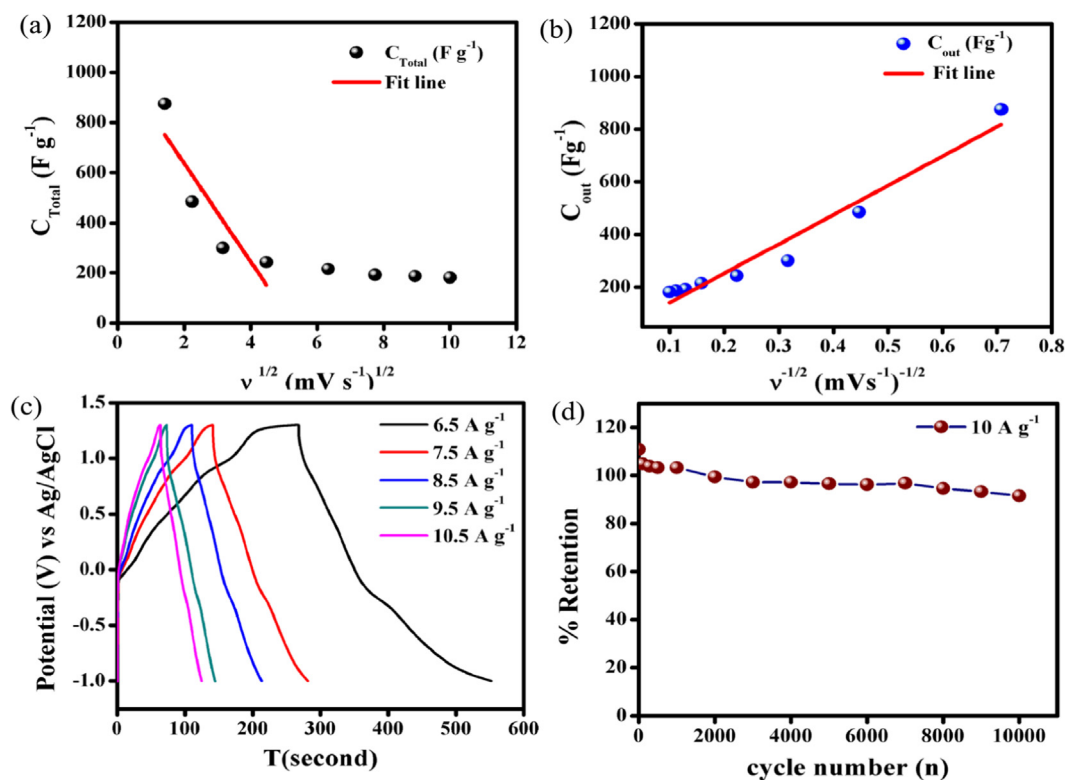


Fig. 6. (a) Specific capacitance vs $v^{1/2}$, (b) Specific capacitance vs $v^{-1/2}$, (c) Galvanostatic charging/ discharging (GCD) curve and (d) Retention (%) plot of NiMn₂O₄ nanoparticles.

surface (C_{out}) of the electrode, which can be expressed as Eq. (12)

$$C_{Total} = C_{in} + C_{out} \text{ (Fg}^{-1}\text{)} \quad (12)$$

Fig. 6(a) represents the linear plot of C_{Total} vs $v^{1/2}$ at lower scan rates, which explains the highest possible specific capacitance value due to uncontrolled ions diffusion by extrapolating the linear plot of the y-axis intercept at $v^{1/2} \rightarrow 0$. At higher scan rates, the experimental data deviates from linear behavior due to the ohmic drop and irreversible redox reaction. Thus, we have fitted the data only at lower scan rates and extrapolating the fitted curve we get the maximum possible specific capacitance (C_{Total}) 1028.2 F g⁻¹. Subsequently, a linear dependence of C_{Total} vs $v^{-1/2}$ plot gives (Fig. 6(b)) the specific capacitance contribution from outer electrode surface at higher scan rates ($v \rightarrow \infty$) and it may be due to controlled ions diffusion into the electrode pores [10,87]. The estimated total specific capacitance (C_T) and outer surface specific capacitance (C_{out}) for the NiMn₂O₄ nanoparticles electrode were 1028.2 F g⁻¹ and 30 F g⁻¹, respectively. The value of specific capacitance contributed by the inner surface (C_{in}) of the electrode was estimated by subtracting C_{out} from C_T , obtaining 998.2 F g⁻¹. Hence, it is confirmed that large number of active sites are present in the inner surface of the NiMn₂O₄ electrode, and the major fraction of the specific capacitance value comes from the contribution of inner sites rather than the outer surface of the electrode, i.e., the charge storage mechanism is strongly controlled by the Faradic adsorption/ desorption process [83,86,88–90].

The electrochemical performance of the electrode made of NiMn₂O₄ nanoparticles was further studied by galvanostatic charge discharge (GCD) process at different current densities (6.5, 7.5, 8.5, 9.5 and 10.5 A g⁻¹). Fig. 6 (c) shows the GCD plots for the potential range -1.0 V to +1.3 V with respect to Ag/AgCl reference electrode, which is consistent with the potential range of CV measurement, i.e. same as CV potential window. The GCD plots indicate the pseudocapacitor type behavior with very low current densities at the potential corresponding to the Faradic reactions. A very small potential drop (IR-drop) is also

observed at the beginning of the discharge curve, even at high current densities, which indicates the NiMn₂O₄ electrode has a very low internal series resistance (R_s) within Na₂SO₄ electrolyte solution, as well as low contact resistance at the interface of current collector and electrolyte solution. A decrease of charging/discharging time with increasing current density can be clearly perceived from the GCD curves, which can be explained considering ion diffusion mechanism. At lower current densities, a large surface area of the electrode is occupied by Na⁺ ions from electrolyte solution as they get enough time to access the maximum active sites of the electrode material, offering higher specific capacitance value. Conversely, due to limited accessibility of the Na⁺ ions inside the electrode material, the specific capacitance of the electrode is lower at higher current densities (see Supplementary Fig. S1(b) and Table S1). The specific capacitance value can also be calculated from the GCD profile at a given current density, using Eq. (13)

$$C_m = \frac{i}{m \left(-\frac{dV}{dt} \right)} \quad (13)$$

where i is the applied current density, dV/dt is the average slope of the discharge curve and m is the effective working electrode mass [2,91].

The long-term cyclic stability of the prepared NiMn₂O₄ electrode is studied up to 10,000 cycles in 1.0 M Na₂SO₄ electrolyte solution at a current density of 10 A g⁻¹, as shown in Fig. 6(d). The specific capacitance retention value of the electrode gradually increases during initial cycles, which is a normal behavior for the electrodes made of metal oxides. The initial increase of specific capacitance occurs due the activation of electroactive sites of the electrode material. The electrodes fabricated using NiMn₂O₄ nanoparticles exhibit very high cycle life of about 91% over 10,000 cycles, indicating the oxides of both the elements (Ni and Mn) play significant roles for the improvement of electrochemical performance of the electrode.

To improve our empathy towards the high specific capacitance of NiMn₂O₄ electrode, the fabricated electrodes were characterized further using electrochemical impedance spectroscopy (EIS). The EIS

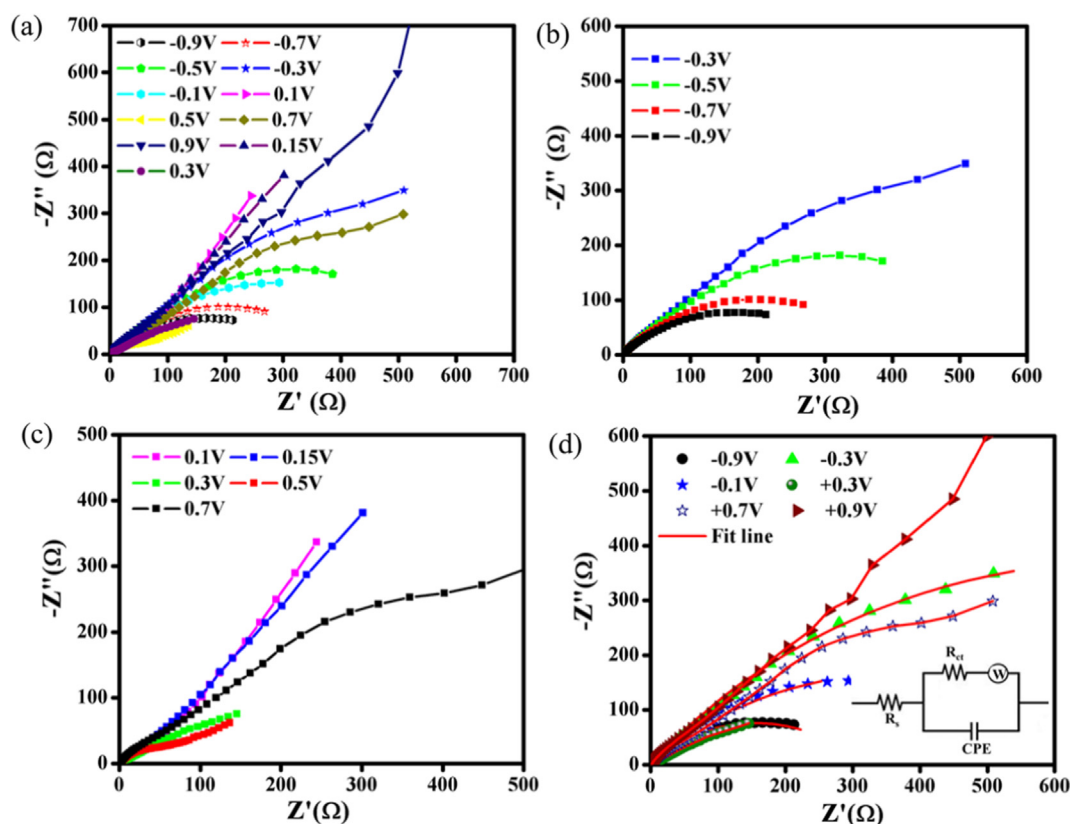


Fig. 7. Electrochemical impedance (EIS) (a) at different potential within CV potential windows, (b) negative potential region, (c) Positive potential region and (d) fitted EIS plot of NiMn₂O₄ nanoparticles.

measurements were carried out in the 0.1 Hz–100 kHz frequency range, with AC perturbation amplitude of 10 mV at different voltages over the potential window of interest. The results of EIS study of the NiMn₂O₄ electrodes over entire frequency range at different voltages are shown in Fig. 7(a). As can be noticed, the impedance behavior of the material is different at different applied voltages, especially near the voltages where the Faradic reaction occurs. The impedance behavior of the electrode at different applied negative (−0.1 V, −0.3 V, −0.5 V, −0.7 V and −0.9 V) and at positive (+0.15 V, +0.30 V, +0.50 V, +0.7 V and +0.90 V) potential are presented in Fig. 7(b) and (c), respectively. It can be seen that at negative potential region (Fig. 7(b)), the NiMn₂O₄ electrode exhibits much higher charge transfer resistance (semicircular Nyquist plots). The decrease of semicircle diameter with the increase of negative potential (Fig. 7(b)) indicates a decrease in charge transfer resistance with the increase of negative potential with respect to Ag/AgCl reference electrode, which leads to a reduction in the Faradic response of the electrode. Similarly, from the impedance behavior of the electrode in positive potential region (Fig. 7(c)) we can notice the frequency dependence linear diffusion process, generally known as Warburg impedance (W_0), which offers a comparative estimation of the diffusion coefficient values [16,18,20,21,92]. In the high frequency region, the increase of semicircular portion in positive potential region may be due to the increase of charge transfer resistance (R_{ct}) with increase of positive applied voltage. The phase angle diagrams (see Supplementary Fig. S1(c and d)) also for this electrode at different applied dc potentials (negative and positive potential windows) indicate that the charge transport process within the electrode material mainly due to redox nature. For ideal capacitive behavior the phase angle approaches to 90° at low frequency and whereas for redox material it is less than 90°. From this phase angle diagrams it can be concluded that the total charge storage arises mainly due to redox nature with a small contribution of double layer storage of the electrode material [10,87,93]. To obtain the charge-transfer parameters of the

NiMn₂O₄ electrode material, the equivalent circuit modeling was further been performed using Z-view software. Fig. 7(d) presents the fitted impedance curves and the equivalent circuit (inset) of the electrode material at different applied voltages in the potential range of interest. From these fitted curves, it is clear that the charge stored in the capacitor has two contributions: contribution of the double layer capacitance, normally known as C_{dl} , and the pseudocapacitance arising from the surface Faradic reaction, C_p . However, in porous electrode material, the constant phase elements (CPE) are typically modeled as capacitor elements. These constant phase elements (CPE) are customarily used to fit the experimental data. The impedance of the capacitor can be represented as

$$Z_{CPE} = 1/(j\omega)^\alpha Y_0$$

where Y_0 generally known as capacitance (C) and α lies between 0.9 and 1.0. Generally, for CPE the α value is less than 1. On real cells the C_{dl} often behaves like a CPE. Several theories have been proposed that CPE arise due to leaky capacitor, porous, surface roughness nature of the material and non-uniform current distribution at the surface etc. to account for the non-ideal nature of C_{dl} . For practical purpose, it is possibly best to treat α as an empirical constant with no real physical basis. Thus, the depressed semi-circular arc in the high frequency region implies the high electrode porosity and roughness nature of the electrode material, which also indicate the presence of large active sites. The constant phase elements, CPE-T and CPE-P have been used to fit the data as shown in equivalent circuit model in Fig. 7(d) inset. The values of different charge transfer parameters determined by equivalent circuit model are presented in Table 1. It can be noticed that the series resistance (R_s) due to the electrolyte solution remains almost constant throughout the used potential window, varies between 0.91 Ω and 1.2 Ω . However, the value of charge transfer resistance (R_{ct}) in parallel combination with CPE changes significantly with applied voltage, offering a minimum value around 0.30 V. On the other hand, the large

Table 1
Values of different charge transfer parameters calculated from equivalent circuit model of NiMn₂O₄ nanoparticles at different potential.

Sl. no	Sample name	Voltage (V)	Rs (Ω)	CPE-T (F cm ⁻²)	CPE-P	Rct (Ω)	W ₀ -R	W ₀ -T	W ₀ -P
1.	NiMn ₂ O ₄	-0.1	0.916	0.0020659	0.55932	695.7	-	-	-
2.		-0.3	1.066	0.0013883	0.6052	1450	-	-	-
3.		-0.5	1.093	0.0014913	0.61502	656	-	-	-
4.		-0.7	1.099	0.0017451	0.60288	390.5	-	-	-
5.		-0.9	1.083	0.0020077	0.5798	310	-	-	-
6.		+0.15	1.146	0.00068776	0.7277	15.74	1900	10.49	0.5111
7.		+0.3	1.154	0.00023148	0.7716	7.571	500.1	32.09	0.37609
8.		+0.5	1.155	0.00049861	0.69072	67.83	308.6	42.19	0.16325
9.		+0.7	1.157	0.00036693	0.70804	120.5	1774	22.44	0.41604
10.		+0.9	1.174	0.00028018	0.72664	1977.8	1419	1.745	0.54516

semicircle indicates the high value of charge transfer resistance between the electrolyte solution and electrode materials at the electrode/electrolyte interface. The charge transfer resistance (R_{ct}) of an electrode can also be expressed with exchange current density (i_0) through Eq. (14)

$$R_{ct} (\text{in ohm}) = \frac{RT}{i_0 F} \quad (14)$$

where R is the gas constant ($J \text{ mol}^{-1} \text{ K}^{-1}$), T is the temperature in Kelvin, i_0 is the exchange current density in Ampere, and F is the Faraday constant (coulomb/mol). Thus the charge transfer resistance (R_{ct}) at a reversible potential can be calculated from Eq. (14). The increase of charge transfer resistance (R_{ct}) can be plainly enlightened on the basis of a decrease in exchange current density due to a decrease in Faradic reaction rate. The variation of R_{ct} with different applied potential (Table 1) clearly suggests that the R_{ct} is strongly dependent on applied potential and the NiMn₂O₄ electrode material offers a very low R_{ct} value at a particular redox potential [2,4,25,94].

It is known that for asymmetric supercapacitors (ASCs) the charge stored at two opposite electrodes (positive and negative) should be equal and opposite i.e. $q^+ = q^-$ [54,95,96]. The amount of charge stored by the each electrode generally depends on the specific capacitance (C_m), mass of the electrode (m) and potential windows (ΔV). The ratio of two electrode mass essential to follow:

$$\frac{m_+}{m_-} = \frac{(C_- \times \Delta E_-)}{(C_+ \times \Delta E_+)}$$

We have measured the CV curve of the activated carbon, AC and NiMn₂O₄ using three electrode system as negative and positive electrode for ACS device application in 1 M Na₂SO₄ electrolyte. We have applied the potential window from 0 V to -1.0 V for AC negative electrode and from 0 V to 0.8 V for NiMn₂O₄ positive electrode, respectively (see Supplementary Fig. S2). The obtained C_m value for AC is 171.8 F g⁻¹ at 2 mV s⁻¹ scan rate in 1 M Na₂SO₄ electrolyte. Fig. 8(a) represents the cyclic voltammograms (CV) of this fabricated ASCs device at different potential windows (0–0.9 V, 0–1.1 V, 0–1.3 V, 0–1.5 V and 0–1.8 V). All CV curves show same nature which indicates that this device can performs within maximum potential window 0–1.8 V without any degradation. Thus, all electrochemical studies have been done within maximum potential window from 0 V to 1.8 V and the CV curves (Fig. 8b) at different scan rates of 2, 5, 10, 20, 40, 60, 80 and 100 mV s⁻¹ show relatively rectangular nature without presence of any redox peaks. It clearly indicates that the charge storage mechanism is mainly due to the electric double layer of the device. The CV profiles also remain almost same without any distortion with increasing scan rates, indicating suitable fast charge-discharge property. To study the rate capability of this ASC device, the GCD test at different current densities (1.0, 1.25, 1.50, 1.75, 2.00, 2.25 and 2.50 A g⁻¹) has been performed. The GCD plots (Fig. 7c) show that the discharge time decreases with increasing current density. For practical purpose it is expected that a good supercapacitor device provides high specific capacitance and high energy density. The relationship between specific

capacitance vs current density (Fig. 8d) of the fabricated ASC device shows that the device delivers maximum specific capacitance of 166.7 F g⁻¹ at current density 1 A g⁻¹. The specific capacitance also decreases when current density increases, since diffusion of electrolyte ions and electrons most likely are restricted due to the time constrain. The EIS plot for this ASC device Fig. 8(e) before and after cycling shows that the spectrum consists of a semicircular portion in high frequency region and a straight line in low frequency region due to ions diffusion. The fitted equivalent circuit also shows in Fig. 8(e) inset. We have fitted the experimental data by suitable equivalent circuit model using Z-view software. Such EIS nature corresponds to the equivalent circuit, which suggests the diffusion control asymmetric behavior of the device [97]. The specific energy and power densities of the ASC have been calculated from the discharge curves at different current densities in the voltage window of 0–1.8 V and the Ragone plot is shown in Fig. 8(f). This device delivers offers specific energy density and power density of 75.01 W h kg⁻¹ and 2250.91 W kg⁻¹, respectively. The long term cycling stability (Fig. 8(g)) of this device for 2000 cycles has also been investigated by GCD between voltage window 0–1.8 V at a constant current density 2.5 A g⁻¹. The GCD curves (Fig. 8g (inset)) follow the same nature during the full cycles. The ASC device configuration (Fig. 8(h)) presents a columbic efficiency 97.6% indicating that the device is suitable for high-performance supercapacitor applications in future.

4. Conclusions

In summary, utilizing a facile and economic sol-gel route, we could synthesize NiMn₂O₄ nanoparticles of ~8 nm average diameter in phase pure spinel structure for the first time. The agglomerated spinel nanoparticles generate highly porous structures, which can be utilized to fabricate working electrodes of electrochemical supercapacitors. The electrodes made of NiMn₂O₄ nanoparticles possess excellent charge storage characteristics, with specific capacitance of up to 875 F g⁻¹ attainable at a scan rate of 2 mV s⁻¹ in 1.0 M Na₂SO₄ electrolyte solution. The coexistence of Ni and Mn in the lattice of this binary oxide is seen to have a positive effect on the improvement of electrochemical charge storage capability of the electrodes due to enhanced electronic conductivity. Porous texture and high electronic conductivity of these binary oxide nanostructures make them attractive for applications in energy storage devices. Through electrochemical impedance spectroscopic (EIS) study, we could explain the charge storage mechanism in the electrodes made of NiMn₂O₄ nanoparticles with the help of equivalent circuit model. The working electrodes made of spinel structure NiMn₂O₄ nanoparticles possess very high specific capacitance, good cyclic stability and excellent asymmetric supercapacitor (ASC) device performance. Moreover, the environmentally-friendly synthesis technique utilized for the synthesis of the nanoparticles makes them very attractive material for the fabrication of high performance electrodes applicable for energy storage devices of future generation.

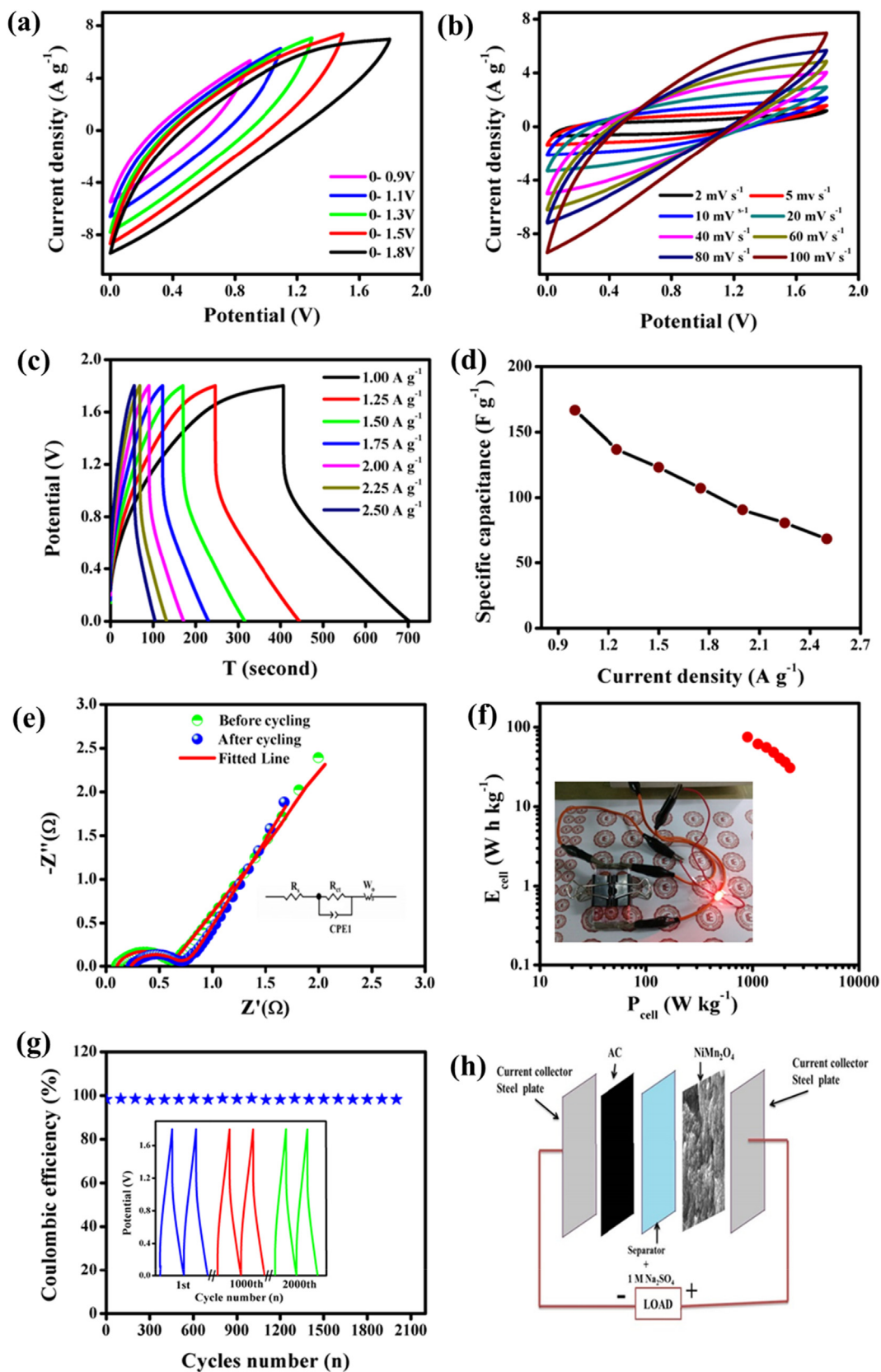


Fig. 8. (a) CV curves at different potential windows, (b) CV curves at different scan rates, (c) GCD curves at different current densities, (d) specific capacitance vs current density plots, (e) EIS plots before and after cycling, (f) Ragone plot, (g) Coulombic efficiency and (h) schematic diagram of ASC device of NiMn₂O₄ nanoparticles.

Acknowledgements

A. Ray (File No.–09/096(0927)/2018-EMR-I) and S. Saha (File No.–09/096(0898)/2017-EMR-I) wish to thank CSIR, Government of India for financial support. S. Das is thankful to the Department of Science and Technology (DST), Government of India, for providing research support through the ‘INSPIRE Faculty Award’ (IFA13-PH-71). A. Roy (IF140920) is also thankful to the Department of Science and Technology (DST), INSPIRE, Government of India, for providing research support through the ‘INSPIRE Fellowship’.

Appendix A. Supplementary material

Supplementary data associated with this article can be found, in the online version, at <https://doi.org/10.1016/j.apsusc.2018.08.259>.

References

- [1] K. Xu, J. Yang, S. Li, Q. Liu, J. Hu, Facile synthesis of hierarchical mesoporous NiCo₂O₄ nanoflowers with large specific surface area for high-performance supercapacitors, *Mater. Lett.* 187 (2017) 129–132, <https://doi.org/10.1016/j.matlet.2016.10.083>.
- [2] A. Ray, A. Roy, S. Bhattacharjee, S. Jana, C.K. Ghosh, C. Sinha, S. Das, Correlation between the dielectric and electrochemical properties of TiO₂-V₂O₅ nanocomposite for energy storage application, *Electrochim. Acta* 266 (2018) 404–413, <https://doi.org/10.1016/j.electacta.2018.02.033>.
- [3] K.V. Sankar, S.C. Lee, Y. Seo, C. Ray, S. Liu, A. Kundu, S.C. Jun, Binder-free cobalt phosphate one-dimensional nanograsses as ultrahigh-performance cathode material for hybrid supercapacitor applications, *J. Power Sources* 373 (2018) 211–219, <https://doi.org/10.1016/j.jpowsour.2017.11.013>.
- [4] J. Tie, J. Han, G. Diao, J. Liu, Z. Xie, G. Cheng, M. Sun, L. Yu, Controllable synthesis of hierarchical nickel cobalt sulfide with enhanced electrochemical activity, *Appl. Surf. Sci.* 435 (2018) 187–194, <https://doi.org/10.1016/j.apsusc.2017.11.086>.
- [5] M.R. Das, A. Roy, S. Mpelane, A. Mukherjee, P. Mitra, S. Das, Influence of dipping cycle on SILAR synthesized NiO thin film for improved electrochemical performance, *Electrochim. Acta* 273 (2018) 105–114, <https://doi.org/10.1016/j.electacta.2018.04.024>.
- [6] L. Shen, L. Du, S. Tan, Z. Zang, C. Zhao, W. Mai, Flexible electrochromic supercapacitor hybrid electrodes based on tungsten oxide films and silver nanowires, *Chem. Commun.* 52 (2016) 6296–6299, <https://doi.org/10.1039/c6cc01139j>.
- [7] D. Majumdar, N. Baugh, S.K. Bhattacharya, Ultrasound assisted formation of reduced graphene oxide-copper (II) oxide nanocomposite for energy storage applications, *Colloids Surf. A Physicochem. Eng. Asp.* 512 (2017) 158–170, <https://doi.org/10.1016/j.colsurfa.2016.10.010>.
- [8] I.Y.Y. Bu, R. Huang, Fabrication of CuO-decorated reduced graphene oxide nanosheets for supercapacitor applications, *Ceram. Int.* 43 (2017) 45–50, <https://doi.org/10.1016/j.ceramint.2016.08.136>.
- [9] F. Wang, G. Li, J. Zheng, J. Ma, C. Yang, Q. Wang, Microwave synthesis of three-dimensional nickel cobalt sulfide nanosheets grown on nickel foam for high-performance asymmetric supercapacitors, *J. Colloid Interface Sci.* 516 (2018) 48–56, <https://doi.org/10.1016/j.jcis.2018.01.038>.
- [10] A. Roy, A. Ray, S. Saha, S. Das, Investigation on energy storage and conversion properties of multifunctional PANI-MWCNT composite, *Int. J. Hydrogen Energy* 43 (2018) 7128–7139, <https://doi.org/10.1016/j.ijhydene.2018.02.153>.
- [11] X. He, R. Li, J. Liu, Q. Liu, R.R. Chen, D. Song, J. Wang, Hierarchical FeCo₂O₄@NiCo layered double hydroxide core/shell nanowires for high performance flexible all-solid-state asymmetric supercapacitors, *Chem. Eng. J.* 334 (2018) 1573–1583, <https://doi.org/10.1016/j.cej.2017.11.089>.
- [12] A. Mohammadi, N. Arsalani, A.G. Tabrizi, S.E. Moosavifard, Z. Naqshbandi, L.S. Ghadimi, Engineering rGO-CNT wrapped Co₃S₄ nanocomposites for high-performance asymmetric supercapacitors, *Chem. Eng. J.* 334 (2018) 66–80, <https://doi.org/10.1016/j.cej.2017.10.029>.
- [13] J. Tan, Y. Han, L. He, Y. Dong, X. Xu, D. Liu, H. Yan, Q. Yu, C. Huang, L. Mai, In situ nitrogen-doped mesoporous carbon nanofibers as flexible freestanding electrodes for high-performance supercapacitors, *J. Mater. Chem. A* 5 (2017) 23620–23627, <https://doi.org/10.1039/c7ta07024a>.
- [14] Y. Yang, L. He, C. Tang, P. Hu, X. Hong, M. Yan, Y. Dong, X. Tian, Q. Wei, L. Mai, Improved conductivity and capacitance of interdigital carbon microelectrodes through integration with carbon nanotubes for micro-supercapacitors, *Nano Res.* 9 (2016) 2510–2519, <https://doi.org/10.1007/s12274-016-1137-3>.
- [15] T.-H. Wu, D. Hesp, V. Dhanak, C. Collins, F. Braga, L.J. Hardwick, C.-C. Hu, Charge storage mechanism of activated manganese oxide composites for pseudocapacitors, *J. Mater. Chem. A* 3 (2015) 12786–12795, <https://doi.org/10.1039/C5TA03334A>.
- [16] J. Deng, L. Kang, G. Bai, Y. Li, P. Li, X. Liu, Y. Yang, F. Gao, W. Liang, Solution combustion synthesis of cobalt oxides (Co₃O₄ and Co₃O₄/CoO) nanoparticles as supercapacitor electrode materials, *Electrochim. Acta* 132 (2014) 127–135, <https://doi.org/10.1016/j.electacta.2014.03.158>.
- [17] Y. Xia, G. Wang, X. Zhang, B. Wang, H. Wang, General access to metal oxide (Metal = Mn, Co, Ni) double-layer nanospheres for application in lithium ion batteries and supercapacitors, *Electrochim. Acta* 220 (2016) 643–653, <https://doi.org/10.1016/j.electacta.2016.10.114>.
- [18] S. Chen, G. Yang, H. Zheng, Aligned Ni-Co-Mn oxide nanosheets grown on conductive substrates as binder-free electrodes for high capacity electrochemical energy storage devices, *Electrochim. Acta* 220 (2016) 296–303, <https://doi.org/10.1016/j.electacta.2016.10.119>.
- [19] Z. Yan, C. Guo, F. Yang, C. Zhang, Y. Mao, S. Cui, Y. Wei, L. Hou, L. Xu, Cliff-like NiO/Ni₃S₂ directly grown on Ni foam for battery-type electrode with high area capacity and long cycle stability, *Electrochim. Acta* 251 (2017) 235–243, <https://doi.org/10.1016/j.electacta.2017.08.102>.
- [20] M. Ihsan, Q. Meng, L. Li, D. Li, H. Wang, K.H. Seng, Z. Chen, S.J. Kennedy, Z. Guo, H.K. Liu, V₂O₅/mesoporous carbon composite as a cathode material for lithium-ion batteries, *Electrochim. Acta* 173 (2015) 172–177, <https://doi.org/10.1016/j.electacta.2015.05.060>.
- [21] B. Pandit, D.P. Dubal, B.R. Sankapal, Large scale flexible solid state symmetric supercapacitor through inexpensive solution processed V₂O₅ complex surface architecture, *Electrochim. Acta* 242 (2017) 382–389, <https://doi.org/10.1016/j.electacta.2017.05.010>.
- [22] J. Lin, H. Jia, H. Liang, S. Chen, Y. Cai, J. Qi, C. Qu, J. Cao, W. Fei, J. Feng, Hierarchical CuCo₂S₄@NiMn-layered double hydroxide core-shell hybrid arrays as electrodes for supercapacitors, *Chem. Eng. J.* 336 (2018) 562–569, <https://doi.org/10.1016/j.cej.2017.12.055>.
- [23] C. Yin, L. He, Y. Wang, Z. Liu, G. Zhang, K. Zhao, C. Tang, M. Yan, Y. Han, L. Mai, Pyrolyzed carbon with embedded NiO/Ni nanospheres for applications in micro-electrodes, *RSC Adv.* 6 (2016) 43436–43441, <https://doi.org/10.1039/C6RA06864B>.
- [24] S. Ardizzone, G. Fregonara, S. Trasatti, “Inner” and “outer” active surface of RuO₂ electrodes, *Electrochim. Acta* (1990), [https://doi.org/10.1016/0013-4686\(90\)85068-X](https://doi.org/10.1016/0013-4686(90)85068-X).
- [25] T. Cheng, W. Li, B. Yu, M. He, L. Cao, X. Li, X. Zheng, Z. Ren, Facile synthesis of hollow Fe₂O₃ nanotubes on nitrogen-doped graphene and their electrochemical performances, *Ionics* (Kiel). 23 (2017) 3203–3210, <https://doi.org/10.1007/s11581-017-2123-9>.
- [26] H. Liang, J. Lin, H. Jia, S. Chen, J. Qi, J. Cao, T. Lin, W. Fei, J. Feng, Hierarchical NiCo-LDH@NiOOH core-shell heterostructure on carbon fiber cloth as battery-like electrode for supercapacitor, *J. Power Sources* 378 (2018) 248–254, <https://doi.org/10.1016/j.jpowsour.2017.12.046>.
- [27] G. Liu, J. Shao, Y. Gao, Z. Chen, Q. Qu, One-pot syntheses of spinel AB₂O₄ (A = Ni or Co, B = Mn or Fe) microspheres with different hollow interiors for supercapacitors application, *Chinese J. Chem.* 35 (2017) 67–72, <https://doi.org/10.1002/cjoc.201600219>.
- [28] Y. Ouyang, Y. Feng, H. Zhang, L. Liu, Y. Wang, Designing sandwiched and crystallized NiMn₂O₄/C arrays for enhanced sustainable electrochemical energy storage, *ACS Sustain. Chem. Eng.* 5 (2017) 196–205, <https://doi.org/10.1021/acssuschemeng.6b01249>.
- [29] J. Yao, Y. Gong, S. Yang, P. Xiao, Y. Zhang, K. Keyshar, G. Ye, S. Ozden, R. Vajtai, P.M. Ajayan, CoMoO₄ nanoparticles anchored on reduced graphene oxide nanocomposites as anodes for long-life lithium-ion batteries, *ACS Appl. Mater. Interfaces* 6 (2014) 20414–20422, <https://doi.org/10.1021/am505983m>.
- [30] Y. Dong, Y. Deng, J. Zeng, H. Song, S. Liao, A high-performance composite ORR catalyst based on the synergy between binary transition metal nitride and nitrogen-doped reduced graphene oxide, *J. Mater. Chem. A* 5 (2017) 5829–5837, <https://doi.org/10.1039/C6TA10496G>.
- [31] L. Chen, L. Chen, Q. Ai, D. Li, P. Si, J. Feng, L. Zhang, Y. Li, J. Lou, L. Ci, Flexible all-solid-state supercapacitors based on freestanding, binder-free carbon nanofibers@polypyrrole@graphene film, *Chem. Eng. J.* 334 (2018) 184–190, <https://doi.org/10.1016/j.cej.2017.10.038>.
- [32] L.L. Xing, K.J. Huang, S.X. Cao, H. Pang, Chestnut shell-like Li₄Ti₅O₁₂ hollow spheres for high-performance aqueous asymmetric supercapacitors, *Chem. Eng. J.* 332 (2018) 253–259, <https://doi.org/10.1016/j.cej.2017.09.084>.
- [33] W. Kang, Y. Tang, W. Li, X. Yang, H. Xue, Q. Yang, C.-S. Lee, High interfacial storage capability of porous NiMn₂O₄/C hierarchical tremella-like nanostructures for the lithium ion battery anode, *Nanoscale* 7 (2015) 225–231, <https://doi.org/10.1039/C4NR04031G>.
- [34] T. Larbi, L. Ben Said, A. Ben Daly, B. Oumi, A. Labidi, M. Amlouk, Ethanol sensing properties and photocatalytic degradation of methylene blue by Mn₃O₄, NiMn₂O₄ and alloys of Ni-manganates thin films, *J. Alloys Compd.* 686 (2016) 168–175, <https://doi.org/10.1016/j.jallcom.2016.06.001>.
- [35] M.Y. Arsent'ev, N.Y. Koval'ko, A.V. Shmigel', P.A. Tikhonov, M.V. Kalinina, NiMn₂O₄ spinel as a material for supercapacitors with a pseudocapacity effect, *Glas. Phys. Chem.* 43 (2017) 376–379, <https://doi.org/10.1134/S1087659617040022>.
- [36] S. Maiti, A. Pramanik, T. Dhawa, M. Sreemany, S. Mahanty, Bi-metal organic framework derived nickel manganese oxide spinel for lithium-ion battery anode, *Mater. Sci. Eng. B Solid-State Mater. Adv. Technol.* 229 (2018) 27–36, <https://doi.org/10.1016/j.mseb.2017.12.018>.
- [37] H. Nan, W. Ma, Z. Gu, B. Geng, X. Zhang, Hierarchical NiMn₂O₄@CNT nanocomposites for high-performance asymmetric supercapacitors, *RSC Adv.* 5 (2015) 24607–24614, <https://doi.org/10.1039/C5RA00979K>.
- [38] J. Dong, G. Lu, F. Wu, C. Xu, X. Kang, Z. Cheng, Facile synthesis of a nitrogen-doped graphene flower-like MnO₂ nanocomposite and its application in supercapacitors, *Appl. Surf. Sci.* 427 (2018) 986–993, <https://doi.org/10.1016/j.apsusc.2017.07.291>.
- [39] H. Yin, C. Song, Y. Wang, S. Li, M. Zeng, Z. Zhang, Z. Zhu, K. Yu, Influence of morphologies and pseudocapacitive contributions for charge storage in V₂O₅ micro/nano-structures, *Electrochim. Acta* 111 (2013) 762–770, <https://doi.org/10.1016/j.electacta.2013.08.005>.
- [40] Y. Zhang, F. Wang, H. Zhu, D. Zhang, J. Chen, Elongated TiO₂ nanotubes directly

- grown on graphene nanosheets as an efficient material for supercapacitors and absorbents, *Compos. Part A Appl. Sci. Manuf.* 101 (2017) 297–305, <https://doi.org/10.1016/j.compositesa.2017.06.026>.
- [41] H. Wang, H. Yi, X. Chen, X. Wang, One-step strategy to three-dimensional graphene/VO₂ nanobelt composite hydrogels for high performance supercapacitors, *J. Mater. Chem. A* 2 (2014) 1165–1173, <https://doi.org/10.1039/c3ta13932h>.
- [42] S. Dutta, S. Bandyopadhyay, A. Dutta, S.K. Pradhan, Microstructure and electrical transport phenomenon of yttria alloyed nanocrystalline ceria solid solution synthesized by mechanical alloying, *Mater. Res. Bull.* 93 (2017) 333–341, <https://doi.org/10.1016/j.materresbull.2017.05.028>.
- [43] S. De, A. Das, D. Das, S. Chatterjee, Structural and magnetic studies of Fe-doped Co₂V₂O₇, *AIP Conference Proceed.* 1832 (2017) 130035, <https://doi.org/10.1063/1.4980755>.
- [44] S. Kundu, B. Satpati, T. Kar, S.K. Pradhan, Microstructure characterization of hydrothermally synthesized PANI/V₂O₅-nH₂O heterojunction photocatalyst for visible light induced photodegradation of organic pollutants and non-absorbing colorless molecules, *J. Hazard. Mater.* 339 (2017) 161–173, <https://doi.org/10.1016/j.jhazmat.2017.06.034>.
- [45] A. Nandy, A. Dutta, S.K. Pradhan, Microstructure correlated electrical conductivity of manganese alloyed nanocrystalline cubic zirconia synthesized by mechanical alloying, *Adv. Powder Technol.* 28 (2017) 618–628, <https://doi.org/10.1016/j.apt.2016.11.014>.
- [46] A. Nandy, T. Kar, S.R. Bhattacharyya, D. Das, S.K. Pradhan, Alteration of magnetic behavior and microstructural distortion of EuMnO₃ by partial substitution of Eu with monovalent Na, *J. Alloys Compd.* 715 (2017) 214–223, <https://doi.org/10.1016/j.jallcom.2017.04.278>.
- [47] S. Saha, A. Nandy, S.K. Pradhan, A.K. Meikap, Electrical transport and dielectric modulus formalism of CuO doped ZrO₂ partially stabilized solid solution, *Mater. Res. Bull.* 88 (2017) 272–280, <https://doi.org/10.1016/j.materresbull.2017.01.003>.
- [48] A.M. Navarro-Suárez, N. Casado, J. Carretero González, D. Mecerreyes, T. Rojo, Full-cell quinone/hydroquinone supercapacitors based on partially reduced graphite oxide and lignin/PEDOT electrodes, *J. Mater. Chem. A* (2017), <https://doi.org/10.1039/C7TA00527J>.
- [49] P.D. Astudillo, D.P. Valencia, M.A. González-Fuentes, B.R. Díaz-Sánchez, C. Frontana, F.J. González, Electrochemical and chemical formation of a low-barrier proton transfer complex between the quinone dianion and hydroquinone, *Electrochim. Acta* 81 (2012) 197–204, <https://doi.org/10.1016/j.electacta.2012.07.078>.
- [50] X. Ji, C.E. Banks, D.S. Silvester, A.J. Wain, R.G. Compton, Electrode kinetic studies of the hydroquinone-benzoquinone system and the reaction between hydroquinone and ammonia in propylene carbonate: Application to the indirect electroanalytical sensing of ammonia, *J. Phys. Chem. C* 111 (2007) 1496–1504, <https://doi.org/10.1021/jp066704y>.
- [51] B. Pandit, D.P. Dubal, P. Gómez-Romero, B.B. Kale, B.R. Sankapal, V₂O₅ encapsulated MWCNTs in 2D surface architecture: complete solid-state bendable highly stabilized energy efficient supercapacitor device, *Sci. Rep.* 7 (2017) 43430, <https://doi.org/10.1038/srep43430>.
- [52] M. Abdollahifar, S.S. Huang, Y.H. Lin, Y.C. Lin, B.Y. Shih, H.S. Sheu, Y.F. Liao, N.L. Wu, High-performance carbon-coated ZnMn₂O₄ nanocrystallite supercapacitors with tailored microstructures enabled by a novel solution combustion method, *J. Power Sources* 378 (2018) 90–97, <https://doi.org/10.1016/j.jpowsour.2017.12.022>.
- [53] X. Hong, L. He, X. Ma, W. Yang, Y. Chen, L. Zhang, H. Yan, Z. Li, L. Mai, Microstructuring of carbon/tin quantum dots via a novel photolithography and pyrolysis-reduction process, *Nano Res.* 10 (2017) 3743–3753, <https://doi.org/10.1007/s12274-017-1587-2>.
- [54] N. Wang, B. Sun, P. Zhao, M. Yao, W. Hu, S. Komarneni, Electrodeposition preparation of NiCo₂O₄ mesoporous film on ultrafine nickel wire for flexible asymmetric supercapacitors, *Chem. Eng. J.* 345 (2018) 31–38, <https://doi.org/10.1016/j.cej.2018.03.147>.
- [55] W. Yang, L. He, X. Tian, M. Yan, H. Yuan, X. Liao, J. Meng, Z. Hao, L. Mai, Carbon-MEMS-based alternating stacked MoS₂@rGO-CNT micro-supercapacitor with high capacitance and energy density, *Small* 13 (2017) 1–8, <https://doi.org/10.1002/sml.201700639>.
- [56] M.S. Islam, C.R.A. Catlow, Structural and electronic properties of NiMn₂O₄, *J. Phys. Chem. Solids* 49 (1988) 119–123, [https://doi.org/10.1016/0022-3697\(88\)90040-6](https://doi.org/10.1016/0022-3697(88)90040-6).
- [57] P.N. Lisboa-Filho, M. Bahout, P. Barahona, C. Moure, O. Peña, Oxygen stoichiometry effects in spinel-type NiMn₂O_{4-x} samples, *J. Phys. Chem. Solids* 66 (2005) 1206–1212, <https://doi.org/10.1016/j.jpcs.2005.03.001>.
- [58] A. Díez, R. Schmidt, A.E. Sagua, M.A. Frechero, E. Matesanz, C. Leon, E. Morán Emilio, Structure and physical properties of nickel manganite NiMn₂O₄ obtained from nickel permanganate precursor, *J. Eur. Ceram. Soc.* 30 (2010) 2617–2624, <https://doi.org/10.1016/j.jeurceramsoc.2010.04.032>.
- [59] J.M.A. Almeida, C.T. Meneses, A.S. de Menezes, R.F. Jardim, J.M. Sasaki, Synthesis and characterization of NiMn₂O₄ nanoparticles using gelatin as organic precursor, *J. Magn. Magn. Mater.* 320 (2008) 304–307, <https://doi.org/10.1016/j.jmmm.2008.02.062>.
- [60] H.M. Lee, K. Lee, C.K. Kim, Electrodeposition of manganese-nickel oxide films on a graphite sheet for electrochemical capacitor applications, *Materials (Basel)* 7 (2014) 265–274, <https://doi.org/10.3390/ma710265>.
- [61] S. Åsbrink, A. Wałkowska, M. Drodz, E. Talik, Physical properties and X-ray diffraction of a NiMn₂O₄ single crystal below and above the ferrimagnetic transition at T_c = 145 K, *J. Phys. Chem. Solids* 58 (1997) 725–729, [https://doi.org/10.1016/S0022-3697\(96\)00198-9](https://doi.org/10.1016/S0022-3697(96)00198-9).
- [62] V.A.M. Brabers, F.M. van Setten, P.S.A. Knapen, X-ray photoelectron spectroscopy study of the cation valencies in nickel manganite, *J. Solid State Chem.* 49 (1983) 93–98, [https://doi.org/10.1016/0022-4596\(83\)90220-7](https://doi.org/10.1016/0022-4596(83)90220-7).
- [63] S.Y. Sawant, V.M.S. Venkatar, S.C. Mojumdar, Preparation, thermal, XRD, chemical and FTIR spectral analysis of NiMn₂O₄ nanoparticles and respective precursor, *J. Therm. Anal. Calorim.* 90 (2007) 669–672, <https://doi.org/10.1007/s10973-007-8520-y>.
- [64] J.L. Baudour, F. Bourée, M.A. Fremy, R. Legros, A. Rousset, B. Gillot, Cation distribution and oxidation states in nickel manganites NiMn₂O₄ and Ni_{0.8}Mn_{2.2}O₄ from powder neutron diffraction, *Phys. B Phys. Condens. Matter.* 180–181 (1992) 97–99, [https://doi.org/10.1016/0921-4526\(92\)90672-F](https://doi.org/10.1016/0921-4526(92)90672-F).
- [65] J. Yang, C. Yu, X. Fan, S. Liang, S. Li, H. Huang, Z. Ling, C. Hao, J. Qiu, Electroactive edge site-enriched nickel-cobalt sulfide into graphene frameworks for high-performance asymmetric supercapacitors, *Energy Environ. Sci.* 9 (2016) 1299–1307, <https://doi.org/10.1039/C5EE03633J>.
- [66] Y.V. Kaneti, J. Zhang, Y.-B. He, Z. Wang, S. Tanaka, M.S.A. Hossain, Z.-Z. Pan, B. Xiang, Q.-H. Yang, Y. Yamauchi, Fabrication of an MOF-derived heteroatom-doped Co/CoO/carbon hybrid with superior sodium storage performance for sodium-ion batteries, *J. Mater. Chem. A* 5 (2017) 15356–15366, <https://doi.org/10.1039/C7TA03939E>.
- [67] T. Zhou, Z. Cao, P. Zhang, H. Ma, Z. Gao, H. Wang, Y. Lu, J. He, Y. Zhao, Transition metal ions regulated oxygen evolution reaction performance of Ni-based hydroxides hierarchical nanoarrays, *Sci. Rep.* 7 (2017) 1–9, <https://doi.org/10.1038/srep46154>.
- [68] F.A. Deorsola, S. Andreoli, M. Armandi, B. Bonelli, R. Pirone, Unsupported nanostructured Mn oxides obtained by solution combustion synthesis: textural and surface properties, and catalytic performance in NO_xSCR at low temperature, *Appl. Catal. A Gen.* 522 (2016) 120–129, <https://doi.org/10.1016/j.apcata.2016.05.002>.
- [69] G. George, S. Anandhan, Synthesis and characterisation of nickel oxide nanofibre webs with alcohol sensing characteristics, *RSC Adv.* 4 (2014) 62009–62020, <https://doi.org/10.1039/C4RA11083H>.
- [70] N. Watanabe, H. Nakayama, K. Fukao, F. Munakata, Transport and x-ray photoelectron spectroscopy properties of (Ni_{1-x}Cu_x)Mn₂O₄ and Ni(Mn_{2-y}Cu_y)O₄, *J. Appl. Phys.* 110 (2011) 023519, <https://doi.org/10.1063/1.3606575>.
- [71] J. Zhang, Y. Li, L. Wang, C. Zhang, H. He, Catalytic oxidation of formaldehyde over manganese oxides with different crystal structures, *Catal. Sci. Technol.* 5 (2015) 2305–2313, <https://doi.org/10.1039/C4CY01461H>.
- [72] D. Li, Y. Gong, Y. Zhang, C. Luo, W. Li, Q. Fu, C. Pan, Facile synthesis of carbon nanosphere/NiCo₂O₄ core-shell sub-microspheres for high performance supercapacitor, *Sci. Rep.* 5 (2015) 1–8, <https://doi.org/10.1038/srep12903>.
- [73] T. Das, A. Roy, H. Uiyama, P. Roy, M. Nandi, 2-Hydroxy-naphthyl functionalized mesoporous silica for fluorescence sensing and removal of aluminum ions, *Dalt. Trans.* 46 (2017) 7317–7326, <https://doi.org/10.1039/c7dt00369b>.
- [74] M. Xue, L. Huang, J.-Q. Wang, Y. Wang, L. Gao, J. Zhu, Z.-G. Zou, The direct synthesis of mesoporous structured MnO₂/TiO₂ nanocomposite: a novel visible-light active photocatalyst with large pore size, *Nanotechnology* 19 (2008) 185604, <https://doi.org/10.1088/0957-4484/19/18/185604>.
- [75] Y. Zhou, W. Jiang, S. Xuan, X. Gong, F. Ye, S. Wang, Q. Fang, Asymmetric PS-EA/Ni-Silicate hollow microsphere with a hierarchical porous shell, *J. Mater. Chem. B* 1 (2013) 1414, <https://doi.org/10.1039/c2tb00508e>.
- [76] D.J. Kim, J.W. Yoon, C.S. Lee, Y.-S. Bae, J.H. Kim, Covalent organic framework-derived microporous carbon nanoparticles coated with conducting polypyrrole as an electrochemical capacitor, *Appl. Surf. Sci.* (2018), <https://doi.org/10.1016/j.apsusc.2018.01.103>.
- [77] L. Peng, Y. Liang, H. Dong, H. Hu, X. Zhao, Y. Cai, Y. Xiao, Y. Liu, M. Zheng, Superhierarchical porous carbons derived from mixed biomass wastes by a stepwise removal strategy for high-performance supercapacitors, *J. Power Sources* 377 (2018) 151–160, <https://doi.org/10.1016/j.jpowsour.2017.12.012>.
- [78] A. Ray, A. Roy, P. Sadhukhan, S.R. Chowdhury, P. Maji, S.K. Bhattacharya, S. Das, Electrochemical properties of TiO₂-V₂O₅ nanocomposites as a high performance supercapacitors electrode material, *Appl. Surf. Sci.* 443 (2018) 581–591, <https://doi.org/10.1016/j.apsusc.2018.02.277>.
- [79] W. Wang, N. Zhang, Z. Shi, Z. Ye, Q. Gao, M. Zhi, Z. Hong, Preparation of Ni-Al layered double hydroxide hollow microspheres for supercapacitor electrode, *Chem. Eng. J.* 338 (2018) 55–61, <https://doi.org/10.1016/j.cej.2018.01.024>.
- [80] Q. Gao, X. Wang, Z. Shi, Z. Ye, W. Wang, N. Zhang, Z. Hong, M. Zhi, Synthesis of porous NiCo₂S₄ aerogel for supercapacitor electrode and oxygen evolution reaction electrocatalyst, *Chem. Eng. J.* 331 (2018) 185–193, <https://doi.org/10.1016/j.cej.2017.08.067>.
- [81] D.K. Tiwari, A. Ray, A. Roy, Water Splitting by Using Electrochemical Properties of Material, *Water Remediation, Energy, Environment and Sustainability*, Springer, Singapore, 2018, pp. 135–153.
- [82] L. Mai, H. Li, Y. Zhao, L. Xu, X. Xu, Y. Luo, Z. Zhang, W. Ke, C. Niu, Q. Zhang, Fast ionic diffusion-enabled nanoflake electrode by spontaneous electrochemical pre-intercalation for high-performance supercapacitor, *Sci. Rep.* 3 (2013) 1–8, <https://doi.org/10.1038/srep01718>.
- [83] J. Duay, S.A. Sherrill, Z. Gui, E. Gillette, S.B. Lee, Self-limiting electrodeposition of hierarchical MnO₂ and M(OH)₂/MnO₂ nanofibril/nanowires: mechanism and supercapacitor properties, *ACS Nano* (2013), <https://doi.org/10.1021/mn3056077>.
- [84] J. Wang, J. Polleux, J. Lim, B. Dunn, Pseudocapacitive contributions to electrochemical energy storage in TiO₂ (anatase) nanoparticles, *J. Phys. Chem. C* 111 (2007) 14925–14931, <https://doi.org/10.1021/jp074464w>.
- [85] K. Zhu, Q. Wang, J.H. Kim, A.A. Pesaran, A.J. Frank, Pseudocapacitive lithium-ion storage in oriented anatase TiO₂ nanotube arrays, *J. Phys. Chem. C* 116 (2012) 11895–11899, <https://doi.org/10.1021/jp301884x>.
- [86] V. Augustyn, P. Simon, B. Dunn, Pseudocapacitive oxide materials for high-rate

- electrochemical energy storage, *Energy Environ. Sci* 7 (2014) 1597–1614, <https://doi.org/10.1039/c3ee44164d>.
- [87] A. Roy, A. Ray, S. Saha, M. Ghosh, T. Das, B. Satpati, M. Nandi, S. Das, NiO-CNT composite for high performance supercapacitor electrode and oxygen evolution reaction, *Electrochim. Acta* 283 (2018) 327–337, <https://doi.org/10.1016/j.electacta.2018.06.154>.
- [88] K.V. Sankar, R.K. Selvan, The preparation of MnFe₂O₄ decorated flexible graphene wrapped with PANI and its electrochemical performances for hybrid supercapacitors, *RSC Adv.* 4 (2014) 17555–17566, <https://doi.org/10.1039/c3ra47681b>.
- [89] C.P. De Pauli, S. Trasatti, Electrochemical surface characterization of IrO₂ + SnO₂ mixed oxide electrocatalysts, *J. Electroanal. Chem.* 396 (1995) 161–168, [https://doi.org/10.1016/0022-0728\(95\)03950-L](https://doi.org/10.1016/0022-0728(95)03950-L).
- [90] D. Baronetto, N. Krstajic, S. Trasatti, Reply to “note on a method to interrelate inner and outer electrode areas” by H. Vogt, *Electrochim. Acta.* 39 (1994) 2359–2362, [https://doi.org/10.1016/0013-4686\(94\)E0158-K](https://doi.org/10.1016/0013-4686(94)E0158-K).
- [91] R.A. Dar, G.A. Naikoo, P.K. Kalambate, L. Giri, F. Khan, S.P. Karna, A.K. Srivastava, Enhancement of the energy storage properties of supercapacitors using graphene nanosheets dispersed with macro-structured porous copper oxide, *Electrochim. Acta* 163 (2015) 196–203, <https://doi.org/10.1016/j.electacta.2015.02.123>.
- [92] H. Wang, L. Pilon, Reply to comments on intrinsic limitations of impedance measurements in determining electric double layer capacitances by H. Wang, L.Pilon, *Electrochim. Acta* 76 (2012) 529–531, <https://doi.org/10.1016/j.electacta.2012.05.039>.
- [93] X. Ma, S. Feng, L. He, M. Yan, X. Tian, Y. Li, C. Tang, X. Hong, L. Mai, Rapid, all dry microfabrication of three-dimensional Co₃O₄/Pt nanonetworks for high-performance microsupercapacitors, *Nanoscale* 9 (2017) 11765–11772, <https://doi.org/10.1039/c7nr01789h>.
- [94] B. Pandit, S.R. Dhakate, B.P. Singh, B.R. Sankapal, Free-standing flexible MWCNTs bucky paper: extremely stable and energy efficient supercapacitive electrode, *Electrochim. Acta* 249 (2017) 395–403, <https://doi.org/10.1016/j.electacta.2017.08.013>.
- [95] C. Wang, Z. Guan, Y. Shen, S. Yu, X.Z. Fu, R. Sun, C.P. Wong, Shape-controlled synthesis of CoMoO₄@Co_{1.5}Ni_{1.5}S₄ hybrids with rambutan-like structure for high-performance all-solid-state supercapacitors, *Chem. Eng. J.* 346 (2018) 193–202, <https://doi.org/10.1016/j.cej.2018.03.160>.
- [96] R. Wang, Y. Sui, S. Huang, Y. Pu, P. Cao, High-performance flexible all-solid-state asymmetric supercapacitors from nanostructured electrodes prepared by oxidation-assisted dealloying protocol, *Chem. Eng. J.* 331 (2018) 527–535, <https://doi.org/10.1016/j.cej.2017.09.004>.
- [97] N.R. Chodankar, D.P. Dubal, Y. Kwon, D.-H. Kim, Direct growth of FeCo₂O₄ nanowire arrays on flexible stainless steel mesh for high-performance asymmetric supercapacitor, *NPG Asia Mater.* 9 (2017) 419, <https://doi.org/10.1038/am.2017.145>.